Appl Phys B (2010) 98: 779–789
DOI 10.1007/s00340-009-3856-6

Applied Physics B
Lasers and Optics

Investigation of wavelength-dependent efficiency droop in InGaN light-emitting diodes

J.-R. Chen · Y.-C. Wu · S.-C. Ling · T.-S. Ko · T.-C. Lu · H.-C. Kuo · Y.-K. Kuo · S.-C. Wang

Received: 29 May 2009 / Revised version: 15 October 2009 / Published online: 18 December 2009

Abstract The physical mechanisms leading to the efficiency droop of InGaN/GaN light-emitting diodes (LEDs) are theoretically investigated. We first discuss the effect of Auger recombination loss on efficiency droop by taking different Auger coefficients into account. It is found that the Auger recombination process plays a significant nonradiative part for carriers at typical LED operation currents when the Auger coefficient is on the order of 10^{-30} $cm^6\,s^{-1}$. Furthermore, the InGaN/GaN multiple-quantum-well (MQW) LEDs with varied indium compositions in InGaN quantum wells are studied to analyze the wavelength-dependent efficiency droop. The simulation results show that the wavelength-dependent efficiency droop is caused by several different effects including non-uniform carrier distribution, electron overflow, built-in electrostatic field induced by spontaneous and piezoelectric polarization, and Auger recombination loss. These internal physical mechanisms are the critical factors resulting in the wavelength-dependent efficiency droop in InGaN/GaN MQW LEDs.

J.-R. Chen (✉) · Y.-C. Wu · S.-C. Ling · T.-S. Ko · T.-C. Lu · H.-C. Kuo · S.-C. Wang
Department of Photonics & Institute of Electro-Optical Engineering, National Chiao Tung University, Hsinchu 300, Taiwan
e-mail: jrchen.eo95g@nctu.edu.tw
Fax: +886-3-5716631

T.-C. Lu
Institute of Lighting and Energy Photonics, National Chiao Tung University, Tainan 711, Taiwan

Y.-K. Kuo
Department of Physics, National Changhua University of Education, Changhua 500, Taiwan

1 Introduction

Nitride-based wide band-gap alloys have been widely used in light-emitting devices including light-emitting diodes (LEDs) [1], laser diodes (LDs) [2], and vertical-cavity surface-emitting lasers (VCSELs) [3]. Especially, GaN-based high-brightness LEDs would play an important role in future applications of solid-state lighting [4, 5]. Although GaN-based high-brightness LEDs have been demonstrated by Nakamura et al. in 1995 [1] and the related ultraviolet, blue, and green LEDs have been commercialized in the following years, the efficiency of the state-of-the-art InGaN/GaN LEDs should be further improved for many specific applications which require high current injection operation. However, for InGaN/GaN multiple-quantum-well (MQW) LEDs, it is commonly observed that the efficiency decreases gradually with increasing injection current, which is the so-called efficiency droop phenomenon. The physical mechanism leading to an efficiency droop in InGaN/GaN LEDs is still controversial and different explanations have been proposed in recent years. Since the obvious efficiency droop is not observed in conventional GaAs-based LEDs, it is expected at an instant's glance that the dislocation density may be the main mechanism causing efficiency droop for GaN-based LEDs. Nevertheless, Schubert et al. have demonstrated that dislocation density reduces the overall efficiency but does not affect the efficiency droop [6]. Furthermore, Auger recombination was proposed as the origin of the efficiency droop by Shen et al. [7] since they measured an Auger coefficient of InGaN ranging from 1.4×10^{-30} to 2.0×10^{-30} $cm^6\,s^{-1}$ by photoluminescence (PL) technique. However, the opposite views on the importance of Auger loss were reported by Hader et al. based on fully microscopic many-body models [8]. Recently, Delaney et al. have suggested again that Auger recombination is indeed

an important loss mechanism in wurtzite InGaN in 2009 [9]. Based on rigorous first-principle calculations, they indicated that the calculated Auger coefficients were in good agreement with the values reported by Shen et al. [7]. The calculated results by Hader et al. did not include a critical second conduction band in their study, leading them to conclude that direct Auger losses are negligible in InGaN quantum wells (QWs) [8]. Moreover, experimental results show that the efficiency droop is unrelated to junction temperature according to the temperature-dependent measurement [10] and the comparison of continuous-wave (CW) and pulse measurements [11]. Besides, it has been found that the efficiency droop is not observed from the power-dependent PL measurements when the carrier density is in the same range of the electrically injected one, which reveals that efficiency droop could be mainly related to the carrier injection, transport, and leakage processes [10]. Kim et al. have proposed that the polarization fields in the InGaN/GaN MQW region enable the escape of electrons from the MQW region and thus are the physical origin of the droop [10]. Xie et al. have also claimed that the efficiency droop is caused by severe electron leakage due to the heavy effective mass of holes and low hole injection efficiency [12]. Other mechanisms including carrier delocalization from indium-rich regions [13], and piezoelectric polarization related to electron-hole separation [14], have been proposed as well. Moreover, another interesting study showed that the efficiency droop is more obvious for green InGaN LEDs and decreases toward shorter wavelengths. Based on these experimental results, some studies deduced that the wavelength-dependent efficiency droop might be caused by the current overflow from localized states or the increase of polarization with increasing indium composition in QWs [15–17].

Although the specific physical mechanisms leading to efficiency droop in InGaN/GaN LEDs are still debatable, two physical mechanisms are referred to as the most possible origins. One is Auger recombination [7, 9, 18–20]. It is generally expected that the Auger recombination is not the issue for GaN materials based on the bandgap dependence in other materials [21, 22]. Nevertheless, the Auger coefficient of the GaN materials is measured and estimated from 1×10^{-34} to 5×10^{-28} $\mathrm{cm}^6\,\mathrm{s}^{-1}$ [7–9, 21–24], which indicates that the Auger recombination is still a possible mechanism resulting in the efficiency droop. The other is the energy band profile of the whole active region, which is related to the quantum-well thickness, quantum-barrier thickness, bandgap energy, quantum confined Stark effect (QCSE), etc. Actually, the energy band profile strongly influences the carrier transport mechanism. Therefore, various band profile designs are proposed in order to reduce carrier overflow, eliminate QCSE, and inhibit efficiency droop [10–12, 19, 25, 26]. Nowadays, most publications only indicate one possible mechanism, such as Auger recombination or carrier overflow. In this study, we demonstrate that the efficiency droop in InGaN LEDs is caused by multiple factors. The effects of Auger loss and energy band profile on wavelength-dependent efficiency droop in InGaN LEDs will be systematically investigated by using an advanced device simulation software APSYS, which self-consistently combines QW band structure calculations by 6×6 $k \cdot p$ theory, radiative and nonradiative carrier recombination, and the carrier drift and diffusion model [27]. The influence of Auger loss on the properties of efficiency droop is analyzed and the polarization-induced effects, such as electron leakage current and electron-hole separation in QW, are also systematically investigated. Furthermore, the mutual influence between different physical mechanisms on the efficiency droop is discussed in this study as well.

2 Theoretical method and device structure

In order to develop high-performance InGaN/GaN LEDs, systematic and compact theoretical modeling is a necessary approach to improve existing LED structures and understand internal physical processes, which provides timely and efficient guidance toward the optimal structure design and device parameters. The self-consistent APSYS simulation program combines two-dimensional (2-D) simulations of carrier transport, quantum-well effect, heat flux, etc. The carrier transport model includes drift and diffusion of electrons and holes in devices. Built-in polarization induced by spontaneous and piezoelectric polarization is considered at hetero-interfaces of nitride-related devices. In the quantum wells, self-consistent Poisson and Schrödinger equations are recomputed at every bias point for the states of quantum-well levels and carrier distributions.

The physical model of the InGaN/GaN quantum wells is considered in such a way that the conduction bands are assumed to be decoupled from valence subbands and have isotropic parabolic bands due to the larger bandgap of nitride semiconductor [28–30]. This condition is different from a zinc-blende GaN structure, which has larger Kane matrix parameter and then causes significant coupling between conduction and valence bands [31]. As for the calculation in valence bands, it includes the coupling of the heavy-hole (HH), the light-hole (LH), and the spin-orbit split-off bands, which are calculated by the 6×6 Hamiltonian with envelop function approximation [32, 33]. To obtain the numerical parameters required for $k \cdot p$ calculations for the InGaN and AlGaN materials, a linear interpolation between the parameters of the relevant binary semiconductors is utilized except for the unstrained bandgap energies. The material parameters of the binary semiconductors are taken from the paper by Vurgaftman and Meyer [34]. The unstrained InGaN and

AlGaN bandgap energies can be expressed as

$$E_g(\mathrm{In}_x\mathrm{Ga}_{1-x}\mathrm{N}) = x \cdot E_{g,\mathrm{InN}} + (1-x) \cdot E_{g,\mathrm{GaN}} - b_{\mathrm{InGaN}} \cdot x \cdot (1-x), \tag{1}$$

$$E_g(\mathrm{Al}_x\mathrm{Ga}_{1-x}\mathrm{N}) = x \cdot E_{g,\mathrm{AlN}} + (1-x) \cdot E_{g,\mathrm{GaN}} - b_{\mathrm{AlGaN}} \cdot x \cdot (1-x), \tag{2}$$

where b_{InGaN} and b_{AlGaN} are the bandgap bowing parameters of InGaN and AlGaN, which are 1.4 and 0.7 eV, respectively [34]. The temperature-dependent bandgap energies of the relevant binary semiconductors are calculated using the commonly employed Varshni formula. The spontaneous emission spectrum in active region can be expressed by [35]

$$r_{\mathrm{sp}}(E) = \frac{q^2 h}{2m_0^2 \varepsilon E} D(E) \rho_{\mathrm{red}}(E) |M|^2 f_c^n \left(1 - f_v^m\right), \tag{3}$$

where q is the free electron charge, h is the Planck constant, $|M|^2$ is the momentum matrix element in the strained quantum well, f_c^n and f_v^m are the Fermi functions for the conduction-band states and the valence band states respectively, $D(E)$ is the optical mode density, and $\rho_{\mathrm{red}}(E)$ is the reduced density of states in each subband. The indices n and m denote the electron states in the conduction band and the heavy-hole (light-hole) subband states in the valence band. The momentum matrix element is computed from the integration of the envelope functions obtained from the $k \cdot p$ calculations [28]. The strain tensor ε_{ij} in the well region is comprised of

$$\varepsilon_{xx} = \varepsilon_{yy} = \frac{a_0 - a}{a}, \tag{4}$$

$$\varepsilon_{zz} = -\frac{2C_{13}}{C_{33}} \varepsilon_{xx}, \tag{5}$$

$$\varepsilon_{xy} = \varepsilon_{yz} = \varepsilon_{zx} = 0, \tag{6}$$

where a_0 and a are the lattice constants of the InGaN or AlGaN layers. C_{13} and C_{33} are the stiffness constants. The effects of calculated strain values will directly affect the quantum-well band structures and the interface charge density in each heterojunction of the LED structures [28, 36]. The optical mode density and reduced density of states can be expressed respectively as

$$D(E) = \frac{\varepsilon n_r E^2}{\pi^2 \hbar^3 c^3}, \tag{7}$$

$$\rho_{\mathrm{red}}(E) = \frac{m_r}{\pi \hbar^2 d_z}, \tag{8}$$

where n_r is the index of refraction, c is the speed of light, d_z is the thickness of the quantum well, m_r is the reduced effective mass. To account for the broadening induced by intraband scattering, the Lorentzian lineshape function is used in the expression of the spontaneous emission spectrum, which is given by

$$R_{\mathrm{sp}} = \frac{1}{\pi} \sum_{i,j} \int r_{\mathrm{sp}}(E) \frac{\Gamma}{(E_{ij} - E)^2 + \Gamma^2} \, dE, \tag{9}$$

where $\Gamma = \hbar/\tau$, which represents the broadening due to intraband scattering relaxation time τ, and E_{ij} is the transition energy from the ith conduction band to the jth valence band. To account for the broadening due to scattering, it is assumed that $\tau = 0.1$ ps in the calculations [28–30]. The conduction-band offset ratio $\Delta E_c / \Delta E_g$ for the InGaN/GaN interface is assumed to be 0.6 based on the recent published literature [37–39]. The internal quantum efficiency, η_{int}, characterizing the device performance of a LED is defined as

$$\eta_{\mathrm{int}} = \frac{q}{J} \int R_{\mathrm{sp}}(V) \, dV. \tag{10}$$

Here J is the total current density in the device and V is the volume of the active region. The internal quantum efficiency is considered not only for the competition between the radiative and nonradiative recombination but also for the effect of carrier leakage from the active region.

The physical model of carrier transport is the traditional drift-diffusion model for semiconductors. The specific equations can be expressed as

$$\vec{J}_n(\vec{r}) = q\mu_n n(r) \vec{F}(\vec{r}) + q D_n \nabla n(r), \tag{11}$$

$$\vec{J}_p(\vec{r}) = q\mu_p p(r) \vec{F}(\vec{r}) - q D_p \nabla p(r), \tag{12}$$

where $n(r)$ and $p(r)$ are the electron and hole concentrations, $\vec{J}_n(\vec{r})$ and $\vec{J}_p(\vec{r})$ are the current densities of electrons and holes, $\vec{F}(\vec{r})$ is the electrostatic field, μ_n and μ_p are the mobilities of electrons and holes. The diffusion constants D_n and D_p are replaced by mobilities using the Einstein relation, $D = \mu k_B T/q$. The equations used to describe the semiconductor device behavior are the Poisson equation,

$$\nabla \cdot \left[\varepsilon_0 \varepsilon \vec{F}(\vec{r})\right] = q\left[p(r) - n(r) + p_D(r) - n_A(r) \pm N_f\right] \tag{13}$$

and current continuity equations for electrons and holes,

$$\frac{1}{q} \nabla \cdot \vec{J}_n(\vec{r}) - R_n(r) + G_n(r) = \frac{\partial n(r)}{\partial t}, \tag{14}$$

$$\frac{1}{q} \nabla \vec{J}_p(\vec{r}) + R_p(r) - G_p(r) = -\frac{\partial p(r)}{\partial t}, \tag{15}$$

Table 1 Net surface charge density at each interface of the $In_{0.2}Ga_{0.8}N$/GaN LED

Interface	Built-in charge density
$Al_{0.2}Ga_{0.8}N$ /GaN	-8.8×10^{12} cm^{-2}
GaN/ $Al_{0.2}Ga_{0.8}N$	$+8.8 \times 10^{12}$ cm^{-2}
$In_{0.2}Ga_{0.8}N$ /GaN	$+2.09 \times 10^{13}$ cm^{-2}
GaN/$In_{0.2}Ga_{0.8}N$	-2.09×10^{13} cm^{-2}

where $G_n(r)$ and $R_n(r)$ are the generation rates and recombination rates for electrons, $G_p(r)$ and $R_p(r)$ are the generation rates and recombination rates for holes, respectively. The recombination rate R accounts for radiative and nonradiative channels. The radiative carrier recombination is dependent on the spontaneous emission rate, R_{sp}, and the nonradiative recombination includes Shockley–Read–Hall (SRH), R_{SRH}, and Auger recombination, R_{Aug}. The SRH recombination is directly governed by the defect-related nonradiative SRH lifetime (τ_{SRH}). Defect density and nonradiative lifetime depend on the substrate used and on the growth quality. In this study, we employ a common value of $\tau_{SRH} = 1$ ns in our simulation [40–42]. The Auger recombination rate is given by

$$R_{Aug}(r) = \left[C_n n(r) + C_p p(r)\right]\left[n(r)p(r) - n_0(r)p_0(r)\right], \tag{16}$$

where C_n and C_p are Auger coefficients, $n_0(r)$ and $p_0(r)$ are the equilibrium electron and hole concentration. The effects of the Auger coefficients on the device performance will be discussed in the following sections.

The internal electric field influences the band profile and carrier transport in devices and is affected by the charge distribution, including the electron and hole concentrations, dopant ions $p_D(r)$ and $n_A(r)$, and other fixed charges N_f that are of special importance in nitride-based devices due to the effect of built-in polarization. The built-in polarization induced by spontaneous and piezoelectric polarizations is known to influence the performance of nitride devices. In order to consider the built-in polarization within the interfaces of nitride devices, the method developed by Fiorentini et al. is employed to estimate the built-in polarization, which is represented by fixed interface charges at each heterointerface. They provided explicit rules to calculate the nonlinear polarization for nitride alloys of arbitrary composition [36]. For the InGaN/GaN LEDs under study, the net surface charges at all interfaces are calculated and listed in Table 1. Although the interface charges can be obtained by this theoretical model, experimental investigations often find a weaker built-in polarization than that predicted by theoretical calculation. It is mainly attributed to partial compensation of the built-in polarization by defect and interface charges [43]. Typical reported experimental values are some 20%, 50% or 80% smaller than the theoretically calculated values [44–46]. As a result, 50% of the theoretical polarization values are used in our simulation from the average of the reported values.

A widely used empirical expression for modeling the mobility of electrons and holes is the Caughey–Thomas approximation, which is employed in our calculation and can be expressed as [47]

$$\mu(N) = \mu_{min} + \frac{\mu_{max} - \mu_{min}}{1 + (N/N_{ref})^{\alpha}}, \tag{17}$$

where μ_{min}, μ_{max}, N_{ref}, and α are fitting parameters according to the experimental mobility measurements. We employ this carrier mobility model for binary GaN material in our calculation. The relative parameters are taken from Refs. [48, 49]. As for ternary AlGaN, the analytical expressions for mobility as a function of doping density have been established by Monte Carlo simulation for various nitride alloys [50]. The calculation of the carrier capture and escape from the quantum wells is considered in accordance with the model provided by Romero et al. [51]. As for the parameter of refractive index, the Adachi model is employed to calculate the refractive index values in each layer [52–54]. More description of the physical models utilized in the APSYS simulation program can be found in Refs. [22, 41, 55].

In this simulation, we first assume that the InGaN/GaN LEDs are grown on a 3-μm-thick n-type GaN layer. On top of this GaN layer, the MQW active region consists of five 3-nm-thick $In_{0.2}Ga_{0.8}N$ QWs and 10-nm-thick GaN barriers. A 20-nm-thick p-type $Al_{0.2}Ga_{0.8}N$ electronic blocking layer (EBL) is grown on top of the active region to reduce electron leakage into the p-type GaN layer [56–58]. Finally, a 0.2-μm-thick p-type GaN cap layer is grown to complete the preliminary LED structure. Moreover, in order to investigate the wavelength-dependent efficiency droop, the indium composition in the $In_xGa_{1-x}N$ QW is changed from 10% to 30% to cover the emission wavelength from violet to green. The InGaN/GaN LED area is 300×300 μm^2. The detailed device structure and doping concentrations in each layer are described in Table 2. The doping data in this table give the actual densities of free carriers.

3 Simulation results and discussion

In first instance we will discuss the effects of Auger recombination on efficiency droop in blue $In_{0.2}Ga_{0.8}N$/GaN LEDs. As mentioned in Sect. 1, the Auger coefficients of GaN materials are reported to range from 10^{-34} to 10^{-28} cm^6 s^{-1} based on different theoretical and experimental estimations. Recently, the Auger coefficient in quasi-bulk InGaN layers

Table 2 Layer structure and room-temperature physical parameters of the GaN/AlGaN quantum-well laser under study (d, layer thickness; N_{dop}, doped carrier density; n, refractive index at wavelength 450 nm). The doped carrier density, N_{dop}, represents the actual density of free carriers

Parameter (unit)	d (nm)	N_{dop} (1/cm^3)	n
p-GaN (contact layer)	200	1.2×10^{18}	2.454
p-$Al_{0.25}Ga_{0.75}N$ (blocking layer)	20	4×10^{17}	2.425
n-GaN (barrier layer)	10	2×10^{17}	2.454
i-$Al_{0.2}Ga_{0.8}N$ (quantum well)	3		3.2393
n-GaN (barrier layer)	10	2×10^{17}	2.454
i-$In_{0.2}Ga_{0.8}N$ (quantum well)	3		3.2393
n-GaN (barrier layer)	10	2×10^{17}	2.454
i-$In_{0.2}Ga_{0.8}N$ (quantum well)	3		3.2393
n-GaN (barrier layer)	10	2×10^{17}	2.454
i-$In_{0.2}Ga_{0.8}N$ (quantum well)	3		3.2393
n-GaN (barrier layer)	10	2×10^{17}	2.454
i-$In_{0.2}Ga_{0.8}N$ (quantum well)	3		3.2393
n-GaN (barrier layer)	10	2×10^{17}	2.454
n-GaN	500	5×10^{18}	2.454
n-GaN	2500	5×10^{18}	2.454
sapphire(substrate)	100000		

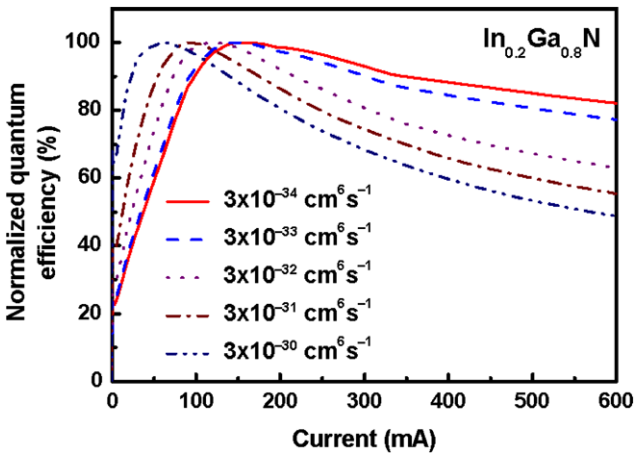

Fig. 1 Normalized quantum efficiency of the $In_{0.2}Ga_{0.8}N$/GaN LED as a function of input current when the calculations take different Auger coefficients into account

was measured from 1.4×10^{-30} to 2.0×10^{-30} cm^6 s^{-1} using a photoluminescence technique [7] and the reported results by Delaney et al. based on rigorous first-principle calculations are also in agreement with these values [9]. Therefore, the Auger coefficient of this magnitude will play a significant nonradiative part for carriers at typical LED operating currents. Figure 1 shows the calculated normalized quantum efficiency of the $In_{0.2}Ga_{0.8}N$/GaN LED as a function of input current when the calculations take different Auger coefficients into account. It is evident that the efficiency droop becomes more obvious with Auger coefficient increasing from 3×10^{-34} to 3×10^{-30} cm^6 s^{-1}. The reduction of the efficiency is nearly 50% with increasing input current to become about 600 mA as using an Auger coefficient of 3×10^{-30} cm^6 s^{-1}. Originally, the efficiency should increase with input current for the ideal case. However, the Auger recombination loss will compete with radiative recombination as the input current increases and thus the efficiency curves first go up to peak values and then gradually decrease. Therefore, the degree of efficiency droop is changed with employing different Auger coefficients in the calculations. Moreover, the peak efficiency value shifts toward lower input current when the larger Auger coefficient is employed in the calculation, which means that the Auger recombination could still be a carrier loss process for the LED under low current injection if the Auger coefficient is really on the order of 10^{-30} cm^6 s^{-1}. To further compare the effects of Auger recombination loss at different injection currents, we plotted the Auger recombination rate within the active region of the $In_{0.2}Ga_{0.8}N$/GaN LED using Auger coefficients of 3×10^{-30} and 3×10^{-34} cm^6 s^{-1} at 30 and 480 mA, respectively, in Fig. 2. The reason for the choice of these current values is to compare the effects of Auger recombination rate under low and high current injection, and thus analyze how this mechanism influences the efficiency droop. The left-hand side of the figure is the n-side of the device. In Fig. 2, the Auger recombination rate calculated using 3×10^{-30} cm^6 s^{-1} is much higher than that calculated using 3×10^{-34} cm^6 s^{-1} even though the input current is 30 mA. Furthermore, the highest Auger recombination rate is always observed in the QW closest to p-side. According to this condition, it is expected that a large number of carriers are within this QW since the Auger recombination rate is in proportion to n^3, where n is the carrier concentration. It is found that this condition is caused by a non-uniform hole distribution within the MQW region, resulting from a

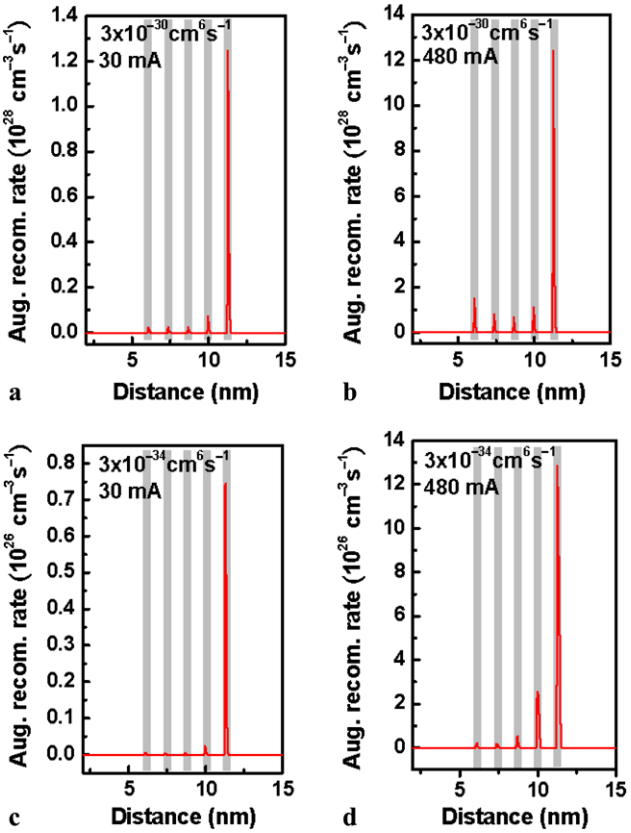

Fig. 2 Auger recombination rate within the active region of the $In_{0.2}Ga_{0.8}N$/GaN LED using Auger coefficients of 3×10^{-30} and 3×10^{-34} $cm^6\ s^{-1}$ at 30 and 480 mA, respectively

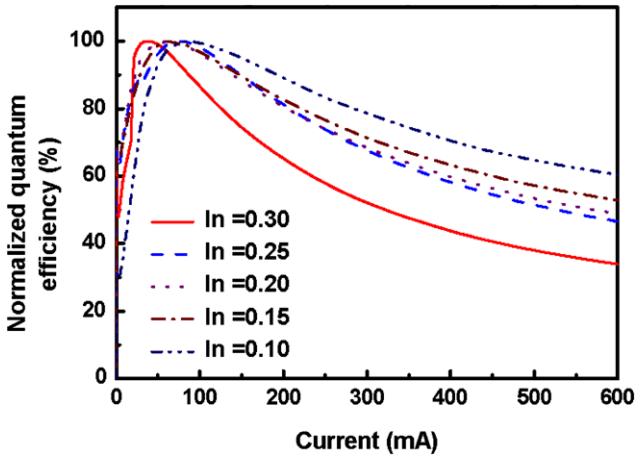

Fig. 3 Normalized quantum efficiency of the InGaN/GaN LEDs with different indium compositions in QWs as a function of input current

large hole effective mass and low hole injection due to relatively low hole concentration, which is in agreement with experimental investigations [12, 59–61]. We will further discuss this issue in the later analysis. According to the calculation results shown in Figs. 1 and 2, the effect of Auger recombination loss combining with serious inhomogeneous distribution of injected carriers plays a significant role in the efficiency droop of InGaN/GaN LEDs when the calculation employs an Auger coefficient of the order of 10^{-30} $cm^6\ s^{-1}$ [7, 9].

Although the specific Auger coefficient of GaN materials may be still debatable, we employ the Auger coefficient of 3×10^{-30} $cm^6\ s^{-1}$ based on the latest report in the following investigation [7, 9]. We further focus our study on the interesting issue of the wavelength-dependent efficiency droop in InGaN LEDs. The LED structures are the same as previously except for the indium composition in QWs which is varied from 10% to 30% to cover the emission wavelength from near ultraviolet to green. Figure 3 shows the calculated normalized quantum efficiency of the InGaN/GaN LEDs with different indium compositions in QWs as a function of input current. It can be observed that the efficiency droop appears to be a strong function of the indium composition in the active region, which has been demonstrated in experimental results [15–17]. In Fig. 3, the efficiency of the $In_xGa_{1-x}N$/GaN LED decreases from 62% to 35% with increasing indium composition in QWs at the injection current of 600 mA. Additionally, the peak efficiency value shifts toward lower input current with increasing indium composition. These calculated results represent that other physical mechanisms will participate in the efficiency droop in addition to the effect of Auger recombination. Practically, there are three possible effects governing the wavelength-dependent efficiency droop in InGaN/GaN LEDs. The first one is the carrier localization originating from the lateral potential fluctuations due to inhomogeneous indium incorporation. Although localization effects improve the radiative efficiency due to the prevention of carriers from nonradiative centers [62], the increased input current may give rise to carriers escaping from the localized states, thus lowering the radiative efficiency owing to the enhanced nonradiative recombination [15–17]. Additionally, with increasing indium composition, the effects of strain and indium phase separation will deteriorate the crystalline quality, which may be an issue for efficiency droop. Nevertheless, Yang et al. demonstrated that crystal quality plays a minor role in light emission and is not responsible for the efficiency droop behaviors in InGaN/GaN green LEDs [17]. Although the indium inhomogeneity is experimentally observed in InGaN QWs and may be the origin of the wavelength-dependent efficiency droop, it is difficult to quantitatively take this effect into account in our calculation. The second one is that the QW energy band profile is affected by the indium composition and the spontaneous and piezoelectric polarizations in QWs. Since the lattice mismatch between GaN barrier and InGaN QW increases with indium composition, the correspondingly increased piezoelectric polarization enhances the tilt of QW potential. The third one is that the Auger coefficient could depend on the indium concentration of the InGaN alloy as reported by Delaney et al. from first-principle

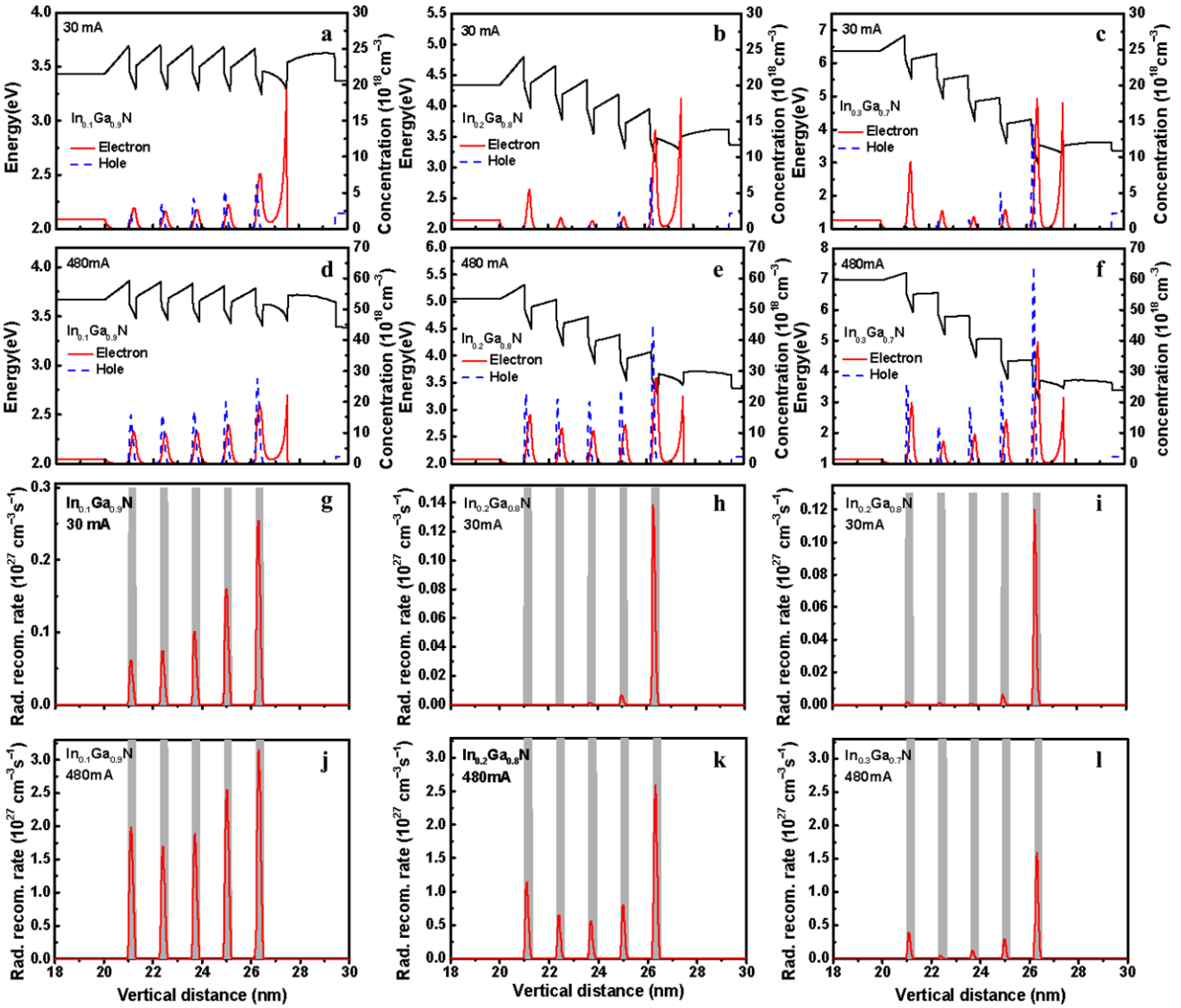

Fig. 4 Vertical profiles of (**a**)–(**f**) electron and hole concentration distribution, conduction-band edge, and (**g**)–(**l**) radiative recombination rate in the active regions of the LED structures with $In_{0.1}Ga_{0.9}N$, $In_{0.2}Ga_{0.8}N$, and $In_{0.3}Ga_{0.7}N$ QWs

calculation [9]. That would induce the additional possibility of the wavelength-dependent efficiency droop. Nevertheless, the experimental measurements of the indium-content dependent Auger coefficients are hardly reported in the literature. Although the process of carriers escaping from the localized states with increasing input current is not considered in our simulation due to the difficulty in quantitatively modeling the randomly position-dependent indium distribution, the wavelength-dependent efficiency droop can still be observed, as shown in Fig. 3. Therefore, we will further discuss the possible physical mechanisms leading to the wavelength-dependent efficiency droop in InGaN/GaN LEDs.

In order to understand the internal physical mechanisms which result in the wavelength-dependent efficiency droop, the vertical profiles of electron and hole concentration distribution, conduction-band edge, and radiative recombination rate in the active regions of the LED structures with $In_{0.1}Ga_{0.9}N$, $In_{0.2}Ga_{0.8}N$, and $In_{0.3}Ga_{0.7}N$ QWs are plotted in Fig. 4, respectively. The gray areas in Figs. 4(g)–4(l) represent the positions of QWs. We investigate these profiles under low injection (30 mA) and high injection (480 mA), respectively, to analyze the possible radiative and nonradiative processes for a wavelength-dependent efficiency droop. In the case of the $In_{0.1}Ga_{0.9}N$/GaN LED, the relatively uniform electron and hole concentration distributions can be observed whatever the injection current is; it may be 30 or 480 mA due to the shallow QWs, as shown in Figs. 4(a) and 4(d). In this condition, all the quantum wells can effectively participate in the radiative recombination process

when the input current is 30 mA, as shown in Fig. 4(g). On the contrary, when the indium composition in the QWs increases, the non-uniform hole concentration distribution is easily observed at low current injection [Figs. 4(b) and 4(c)]. The hole concentration in the QW near the p-side is larger than that in the QW adjacent to the n-side due to the large effective mass of the holes and the deep QWs for the $In_{0.2}Ga_{0.8}N$/GaN and $In_{0.3}Ga_{0.7}N$/GaN LEDs [59–61]. However, under the same injection current the electrons can relatively easily transport through the MQW region. In addition to the effect of barrier height on the non-uniform carrier distribution, the barrier height created by $Al_{0.2}Ga_{0.8}N$ electronic blocking layer is substantially reduced by the high density of positive polarization charges at the interface between the GaN barrier layer and the $Al_{0.2}Ga_{0.8}N$ electronic blocking layer. This condition will lead to the severe accumulation of electrons at this interface due to the attraction of positive charges by Coulomb force, causing strong band bending at this interface, as indicated in Figs. 4(a)–4(f). Consequently, a higher electron concentration at the GaN/$Al_{0.2}Ga_{0.8}N$ interface and in the QW closest to the p-side is observed. Therefore, because of the non-uniform hole distribution and the electron accumulation, most of the radiative recombination occurs only within the first QW close to the p-side when the indium composition in the QWs increases, as shown in Figs. 4(h) and 4(i). This phenomenon is in agreement with experimental observation [61]. Additionally, the effect of band bending at the GaN/$Al_{0.2}Ga_{0.8}N$ interface will reduce the effective energy barrier height and thus significantly enhances the escape of electrons from the active region [10, 63, 64]. Furthermore, when the input current is 480 mA, the electron and hole concentration distributions in the active region of the $In_{0.1}Ga_{0.9}N$/GaN LED are relatively uniform across all the QWs, which correspondingly leads to the similar magnitude of radiative recombination rate in each QW, as shown in Fig. 4(j). Nevertheless, with increasing indium composition in the QWs the non-uniform carrier distribution and radiative recombination rate within the MQWs can still be observed when the injection current is 480 mA [Figs. 4(f) and 4(l)]. The deep QWs and large effective mass of holes cause the significant increase of hole concentration in the QW nearest the *p*-layer under this high current injection. Combining the effect of electron accumulation, the QW closest to *p*-type layer still dominates the radiative recombination process, as shown in Fig. 4(l). Therefore, to enhance all the QWs participating in the radiative recombination process, a more effective hole transport within the MQW region is required, especially for the high-indium-content MQWs.

In addition to the effect of increased barrier height with indium composition in QWs, the piezoelectric polarization induced by lattice mismatch between GaN barrier layer and InGaN QW will also increase with indium composition. Figure 5 shows the calculated interface charge density at the interface between the InGaN QW and the GaN barrier layer as a function of the indium composition. The interface charge density of the $In_{0.3}Ga_{0.7}N$/GaN interface is nearly three and a half times larger than that of the $In_{0.1}Ga_{0.9}N$/GaN interface. In this situation, the built-in polarization causes a strong deformation of the band structure in $In_{0.3}Ga_{0.7}N$/GaN QWs accompanied by an electrostatic field. Therefore, the separation of electrons and holes in $In_{0.3}Ga_{0.7}N$/GaN QWs becomes more obvious than that in $In_{0.1}Ga_{0.9}N$/GaN QWs, as shown in Figs. 4(d) and 4(f). Although the deep QWs can confine higher carrier concentrations, the non-uniform carrier distribution and severe electron–hole separation with increasing indium composition result in low radiative recombination rate in the

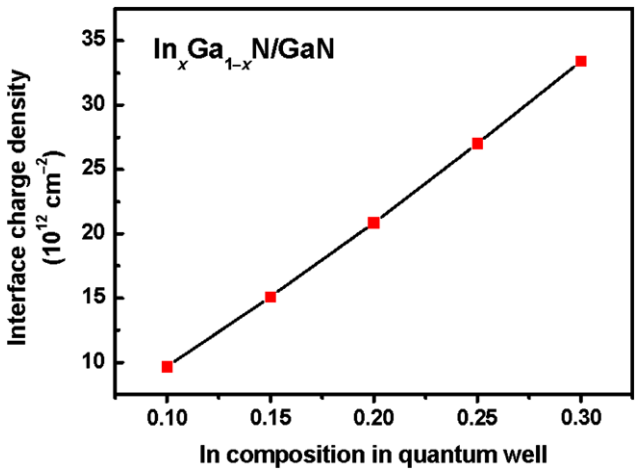

Fig. 5 Calculated interface charge density at the interface between the InGaN QW and the GaN barrier layer as a function of the indium composition

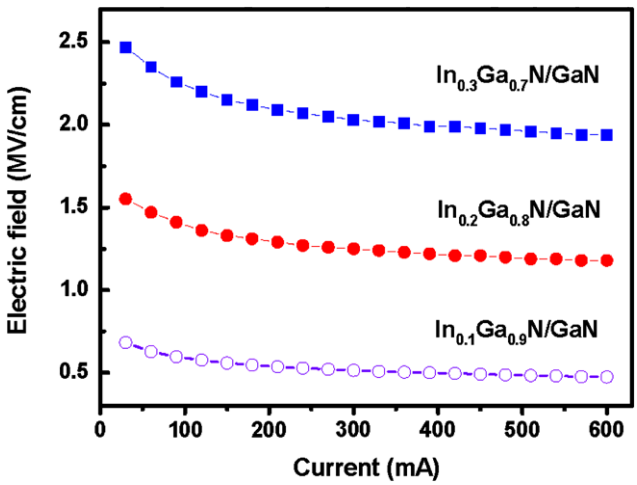

Fig. 6 Internal electric field in the QWs of the LED structures with $In_{0.1}Ga_{0.9}N$, $In_{0.2}Ga_{0.8}N$, and $In_{0.3}Ga_{0.7}N$ QWs, respectively, as a function of input current

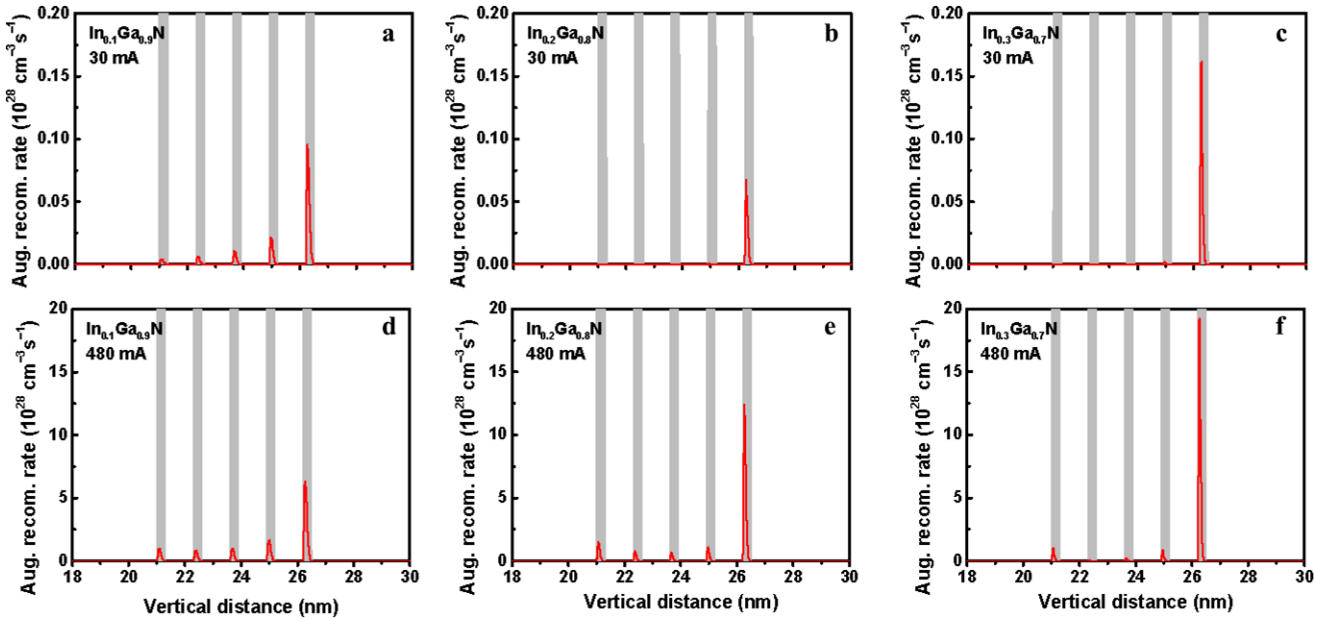

Fig. 8 Auger recombination rate within the active region of InGaN/GaN LEDs with different indium compositions under the injection current of 30 and 480 mA, respectively

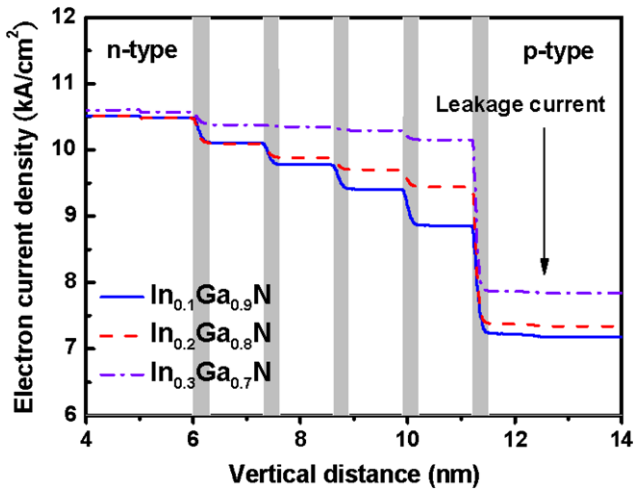

Fig. 7 Vertical electron current density profiles within the active regions of the LEDs with $In_{0.1}Ga_{0.9}N$, $In_{0.2}Ga_{0.8}N$, and $In_{0.3}Ga_{0.7}N$ MQW, respectively, at the input current of 480 mA

$In_{0.3}Ga_{0.7}N$/GaN QWs, as shown in Fig. 4(l). Figure 6 plots the internal electric field in the QWs of the LED structures with $In_{0.1}Ga_{0.9}N$, $In_{0.2}Ga_{0.8}N$, and $In_{0.3}Ga_{0.7}N$ QWs, respectively, as a function of input current. The electric field in these three LEDs decreases with increasing input current due to the screening effect. Nevertheless, the increased input current still cannot completely screen the large built-in polarization, especially for $In_{0.3}Ga_{0.7}N$/GaN QWs [63]. Figure 7 shows the vertical electron current density profiles within the active regions of the LED structures with $In_{0.1}Ga_{0.9}N$, $In_{0.2}Ga_{0.8}N$, and $In_{0.3}Ga_{0.7}N$ QWs, respectively, at the input current of 480 mA. The positions of the QWs are marked with gray areas. The electron current is injected from *n*-type layers into quantum wells and recombines with holes in QWs. Therefore, the electron current density is consumed after passing each QW region. Electron current which overflows to the *p*-type region is viewed as the leakage current. In Fig. 7, the electron leakage current is easily observed under this high driving current for the three LED structures. However, the $In_{0.3}Ga_{0.7}N$ LED reveals a more serious electron leakage current than the other two LEDs. Although the $In_{0.3}Ga_{0.7}N$/GaN LED provides deep QWs in the active region, the relatively light effective mass of electrons, the attraction of positive charges at the GaN/$Al_{0.2}Ga_{0.8}N$ interface [63], the large built-in polarization [10, 14], and the non-uniform hole distribution [12] lead to higher electron leakage current.

As our previous discussion, the Auger recombination process really plays an important role if the Auger recombination coefficient of the GaN materials is on the order of 10^{-30} cm^6 s^{-1}. Therefore, we will further discuss the wavelength-dependent Auger recombination process. Figure 8 shows the Auger recombination rate within the active region of InGaN/GaN LEDs with different indium compositions under the injection current of 30 and 480 mA, respectively. When the input current is 30 mA, the total Auger recombination rate in the QWs of $In_{0.1}Ga_{0.9}N$, $In_{0.2}Ga_{0.8}N$, and $In_{0.3}Ga_{0.7}N$ LEDs, respectively, is comparable. However, the Auger recombination rate of the $In_{0.3}Ga_{0.7}N$ LED is obviously larger than that of the $In_{0.1}Ga_{0.9}N$ LED as the input current is 480 mA. The higher Auger recombination

rate could be one of the mechanisms leading to the severe efficiency droop for the $In_{0.3}Ga_{0.7}N$/GaN LED. Moreover, the highest Auger recombination rate is still within the first QW close to the *p*-side for the $In_{0.3}Ga_{0.7}N$ LED, which is attributed to the severely non-uniform carrier distribution within the MQW region, as discussed previously. As a result, the Auger recombination process may be still one of the possible issues leading to the wavelength-dependent efficiency droop in InGaN/GaN LEDs.

4 Conclusion

Theoretical simulation has been used to investigate the possible physical mechanisms resulting in the efficiency droop in InGaN/GaN LEDs. The calculated results indicate that the effect of Auger recombination loss plays an important role in the efficiency droop of InGaN/GaN LEDs if the Auger coefficient of GaN materials is on the order of 10^{-30} cm^6 s^{-1}. Furthermore, the wavelength-dependent efficiency droop is discussed by using different indium compositions in the InGaN/GaN QWs. According to the simulation results, we deduce that there are four internal physical mechanisms leading to the wavelength-dependent efficiency droop. First, the deep MQWs employed by increasing the indium composition in InGaN/GaN MQWs cause the severely non-uniform carrier distribution, which induces that only the QW close to *p*-side might effectively participate in the radiative recombination. Second, the built-in polarization increases with increasing indium composition due to the lattice-mismatch-induced piezoelectric polarization, which enhances the separation of electrons and holes in QWs and thus reduces the radiative recombination. Third, the effect of electron overflow is more obvious with increasing indium composition in QWs, which originates from the non-uniform carriers distribution and increased built-in polarization in high-indium-content MQWs. Fourth, the Auger recombination loss is higher with increasing indium composition due to the effect of carrier accumulation in the QW closest to *p*-side. Although the effect of carrier localization may be still a possible mechanism of efficiency droop from the viewpoint of practical issue in InGaN materials, the condition of the wavelength-dependent efficiency droop can be observed in the calculation, which means that additional factors summarized as the four effects could result in the wavelength-dependent efficiency droop in InGaN/GaN LEDs.

Acknowledgements This work was supported in part by the MOE ATU program and in part by the National Science Council of the Republic of China under Contracts NSC 98-3114-M-009-001, NSC 96-2221-E-009-094-MY3, NSC 98-2221-E-009-016-MY3, and NSC 96-2112-M-018-007-MY3.

References

1. S. Nakamura, M. Senoh, N. Iwasa, S.-I. Nagahama, Jpn. J. Appl. Phys. **34**, L797 (1995)
2. S. Nakamura, M. Senoh, S.-I. Hagahama, N. Iwasa, T. Yamada, T. Matsushita, H. Kiyoku, Y. Sugimoto, T. Kozaki, H. Umemoto, M. Sano, K. Chocho, Jpn. J. Appl. Phys. **37**, L309 (1998)
3. T.-C. Lu, C.-C. Kuo, H.-C. Kuo, G.-S. Huang, S.-C. Wang, Appl. Phys. Lett. **92**, 141102 (2008)
4. E.F. Schubert, J.K. Kim, Science **308**, 1274 (2005)
5. D.A. Steigerwald, J.C. Bhat, D. Collins, R.M. Fletcher, M.O. Holcomb, M.J. Ludowise, P.S. Martin, S.L. Rudaz, IEEE J. Select. Topics Quantum Electron. **8**, 310 (2002)
6. M.F. Schubert, S. Chhajed, J.K. Kim, E.F. Schubert, D.D. Koleske, M.H. Crawford, S.R. Lee, A.J. Fischer, G. Thaler, M.A. Banas, Appl. Phys. Lett. **91**, 231114 (2007)
7. Y.C. Shen, G.O. Mueller, S. Watanabe, N.F. Gardner, A. Munkholm, M.R. Krames, Appl. Phys. Lett. **91**, 141101 (2007)
8. J. Hader, J.V. Moloney, B. Pasenow, S.W. Koch, M. Sabathil, N. Linder, S. Lutgen, Appl. Phys. Lett. **92**, 261103 (2008)
9. K.T. Delaney, P. Rinke, C.G. Van de Walle, Appl. Phys. Lett. **94**, 191109 (2009)
10. M.-H. Kim, M.F. Schubert, Q. Dai, J.K. Kim, E.F. Schubert, J. Piprek, Y. Park, Appl. Phys. Lett. **91**, 183507 (2007)
11. Y.-L. Li, Y.-R. Huang, Y.-H. Lai, Appl. Phys. Lett. **91**, 181113 (2007)
12. J. Xie, X. Ni, Q. Fan, R. Shimada, Ü. Özgür, H. Morkoç, Appl. Phys. Lett. **93**, 121107 (2008)
13. B. Monemar, B.E. Sernelius, Appl. Phys. Lett. **91**, 181103 (2007)
14. M. Kunzer, M. Baeumler, K. Köhler, C.-C. Leancu, U. Kaufmann, J. Wagner, Phys. Status Solidi A **204**, 236 (2007)
15. Y. Yang, X.A. Cao, C. Yan, IEEE Trans. Electron Devices **55**, 1771 (2008)
16. M. Baeumler, M. Kunzer, R. Schmidt, S. Liu, W. Pletschen, P. Schlotter, K. Köhler, U. Kaufmann, J. Wagner, Phys. Status Solidi A **204**, 1018 (2007)
17. Y. Yang, X.A. Cao, C.H. Yan, Appl. Phys. Lett. **94**, 041117 (2009)
18. N.F. Gardner, G.O. Müller, Y.C. Shen, G. Chen, S. Watanabe, W. Götz, M.R. Krames, Appl. Phys. Lett. **91**, 243506 (2007)
19. M. Maier, K. Köhler, M. Kunzer, W. Pletschen, J. Wagner, Appl. Phys. Lett. **94**, 041103 (2009)
20. K.A. Bulashevich, S.Y. Karpov, Phys. Status Solidi C **5**, 2066 (2008)
21. J. Piprek, S. Nakamura, Inst. Elec. Eng. Proc. Optoelectron. **149**, 145 (2002)
22. J. Piprek, *Semiconductor Optoelectronic Device: Introduction to Physics and Simulation* (Academic Press, San Diego, 2003)
23. P.G. Eliseev, M. Osin'ski, H. Li, I.V. Akimova, Appl. Phys. Lett. **75**, 3838 (1999)
24. M. Shatalov, A. Chitnis, A. Koudymov, J. Zhang, V. Adivarahan, G. Simin, M.A. Khan, Jpn. J. Appl. Phys. **41**, L1146 (2002)
25. J. Xu, M.F. Schubert, A.N. Noemaun, D. Zhu, J.K. Kim, Y. Park, Appl. Phys. Lett. **94**, 011113 (2009)
26. M.F. Schubert, J. Xu, J.K. Kim, E.F. Schubert, M.H. Kim, S. Yoon, S.M. Lee, C. Sone, T. Sakong, Y. Park, Appl. Phys. Lett. **93**, 041102 (2008)
27. APSYS by Crosslight Software, Inc., Burnaby, Canada, 2008. http://www.crosslight.com
28. S.L. Chuang, IEEE J. Quantum Electron. **32**, 1791 (1996)
29. Y.C. Yeo, T.C. Chong, M.-F. Li, W.J. Fan, IEEE J. Quantum Electron. **34**, 526 (1998)
30. Y.C. Yeo, T.C. Chong, M.F. Li, W.J. Fan, J. Appl. Phys. **84**, 1813 (1998)
31. O. Marquardt, D. Mourad, S. Schulz, T. Hickel, G. Czycholl, J. Neugebauer, Phys. Rev. B **78**, 235302 (2008)
32. S.L. Chuang, C.S. Chang, Phys. Rev. B **54**, 2491 (1996)

33. S.L. Chuang, C.S. Chang, Appl. Phys. Lett. **68**, 1657 (1996)
34. I. Vurgaftman, J.R. Meyer, J. Appl. Phys. **94**, 3675 (2003)
35. R.H. Yan, S.W. Corzine, L.A. Coldren, I. Suemune, IEEE J. Quantum Electron. **26**, 213 (1990)
36. V. Fiorentini, F. Bernardini, O. Ambacher, Appl. Phys. Lett. **80**, 1204 (2002)
37. H. Zhang, E.J. Miller, E.T. Yu, C. Poblenz, J.S. Speck, Appl. Phys. Lett. **84**, 4644 (2004)
38. H. Zhang, E.J. Miller, E.T. Yu, C. Poblenz, J.S. Speck, J. Vac. Sci. Technol. B **22**, 2169 (2004)
39. D. Biswas, S. Kumar, T. Das, Thin Solid Films **515**, 4488 (2007)
40. M.F. Huang, T.H. Lu, IEEE J. Quantum Electron. **42**, 820 (2006)
41. Y.K. Kuo, S.H. Yen, J.R. Chen, in *Nitride Semiconductor Devices: Principles and Simulation*, ed. by J. Piprek (Wiley-VCH Verlag GmbH & Co. KGaA, Weinheim, 2007), p. 279, Chap. 13
42. J. Piprek, T. Katona, S.P. DenBaars, S. Li, SPIE Proc. **5366**, 127 (2004)
43. J.P. Ibbetson, P.T. Fini, K.D. Ness, S.P. DenBaars, J.S. Speck, U.K. Mishra, Appl. Phys. Lett. **77**, 250 (2000)
44. S.F. Chichibu, A.C. Abare, M.S. Minsky, S. Keller, S.B. Fleischer, J.E. Bowers, E. Hu, U.K. Mishra, L.A. Coldren, S.P. DenBaars, T. Sota, Appl. Phys. Lett. **73**, 2006 (1998)
45. H. Zhang, E.J. Miller, E.T. Yu, C. Poblenz, J.S. Speck, Appl. Phys. Lett. **84**, 4644 (2004)
46. F. Renner, P. Kiesel, G.H. Dőhler, M. Kneissl, C.G. Van de Walle, N.M. Johnson, Appl. Phys. Lett. **81**, 490 (2002)
47. C.M. Caughey, R.E. Thomas, Proc. IEEE **55**, 2192 (1967)
48. T.T. Mnatsakanov, M.E. Levinshtein, L.I. Pomortseva, S.N. Yurkov, G.S. Simin, M.A. Khan, Solid State Electron. **47**, 111 (2003)
49. F. Schwierz, Solid State Electron. **49**, 889 (2005)
50. M. Farahmand, C. Garetto, E. Bellotti, K.F. Brennan, M. Goano, E. Ghillino, G. Ghione, J.D. Albrecht, P.P. Ruden, IEEE Trans. Electron Devices **48**, 535 (2001)
51. B. Romero, J. Arias, I. Esquivias, M. Cada, Appl. Phys. Lett. **76**, 1504 (2000)
52. S. Adachi, *Physical Properties of III–V Semiconductor Compounds* (Wiley, New York, 1992)
53. T. Peng, J. Piprek, Electron. Lett. **32**, 2285 (1996)
54. G.M. Laws, E.C. Larkins, I. Harrison, C. Molloy, D. Somerford, J. Appl. Phys. **89**, 1108 (2001)
55. J. Piprek, S. Li, in *Optoelectronic Devices: Advanced Simulation and Analysis*, ed. by J. Piprek (Springer, New York, 2005), p. 293, Chap. 10
56. Y.-K. Kuo, Y.-A. Chang, IEEE J. Quantum Electron. **40**, 437 (2006)
57. K. Domen, R. Soejima, A. Kuramata, T. Tanahashi, MRS Internet J. Nitride Semicond. Res. **3**(2) (1998)
58. J.Y. Chang, Y.K. Kuo, J. Appl. Phys. **93**, 4992 (2003)
59. X. Ni, Q. Fan, R. Shimada, Ü. Özgür, H. Morkoç, Appl. Phys. Lett. **93**, 171113 (2008)
60. J.P. Liu, J.-H. Ryou, R.D. Dupuis, J. Han, G.D. Shen, H.B. Wang, Appl. Phys. Lett. **93**, 021102 (2008)
61. A. David, M.J. Grundmann, J.F. Kaeding, N.F. Gardner, T.G. Mihopoulos, M.R. Krames, Appl. Phys. Lett. **92**, 053502 (2008)
62. G. Franssen, S. Grzanka, R. Czernecki, T. Suski, L. Marona, T. Riemann, J. Christen, H. Teisseyre, P. Valvin, P. Lefebvre, P. Perlin, M. Leszczyński, I. Grzegory, J. Appl. Phys. **97**, 103507 (2005)
63. J. Piprek, R. Farrell, S. DenBaars, S. Nakamura, IEEE Photon. Technol. Lett. **18**, 7 (2006)
64. J.-R. Chen, C.-H. Lee, T.-S. Ko, Y.-A. Chang, T.-C. Lu, H.-C. Kuo, Y.-K. Kuo, S.-C. Wang, IEEE J. Lightwave Technol. **26**, 329 (2008)